*Machine Copy for Proofreading, Vol. x, y–z, 2004*

# HUYGENS PRINCIPLE BASED IMAGING OF MULTILAYERED OBJECTS WITH INCLUSIONS

**Navid Ghavami, Gianluigi Tiberi, David J. Edwards, Ahmad Safaai-Jazi, and Agostino Monorchio**

Department of Engineering Science, University of Oxford, Parks Road, Oxford, UK

Fondazione Imago7, Viale del Tirreno, I-56128 Pisa, Italy

Department of Electrical and Computer Engineering, Virginia Tech University, US

Department of Information Engineering, University of Pisa, Via G. Caruso 16, I-56122 Pisa, Italy

**Abstract**—This paper describes the extension of a recently introduced microwave imaging technique for treating multilayered objects with inclusions. The technique is based on the Huygens Principle (HP): Using HP to forward propagate the waves removes the need to solve inverse problems and, consequently, no matrix generation/inversion is required. In addition to its simplicity, the methodology permits the capture of contrast, to the extent in which different material properties within the region of interest can be discriminated in the final image. Specifically, this can be seen as localization of an object inside the medium. It follows that the methodology can identify the presence and location of significant scatterers inside a multilayered volume, without having apriori knowledge on the dielectric properties of the target object. Additionally, an analytically-based approach for analyzing UWB body propagation is presented, where the body is modeled as a 3-layer stratified cylinder with an eccentric inclusion. Validation of the technique through both simulations and measurements on multilayered cylindrical objects with inclusions has been performed.

## 1. INTRODUCTION

In recent years, there has been a growing interest in the development of imaging methods for medical applications. Microwave imaging has been recognized as a promising non-ionizing and non-invasive

alternative screening technology for these application areas. Microwave imaging has attracted increasing attention in the last decade, especially due to its applicability to breast cancer detection. This capability is motivated by the significant contrast in the dielectric properties of normal and malignant tissues at microwave frequencies. At present, there are two main breast imaging techniques employing microwave signals; microwave tomography and UWB radar techniques. Tomographic image reconstruction involves solving a nonlinear inverse scattering problem in order to recover an image of the dielectric properties in the breast [1–3]. Based on the previous works in this area [4, 5], a new analytical approach has recently been introduced by reformulating the inverse scattering problem as an inverse source one. This new approach requires the calculation of both the radiating and the non-radiating parts of the induced currents, and permits an efficient solution of 2D problems [6–8].

The UWB radar approach solves a simpler computational problem by seeking only to identify the significant scatterers inside the target volume [9–13]. Reconstructing the image requires beamforming techniques of varying complexity. Current beamforming techniques use time domain processing algorithms; a common method is confocal imaging that employs simple delay-and-sum beamforming [8, 10]. However, while being computationally inexpensive, confocal imaging causes major problems in imaging spaces which possess volumes of varying dielectric constant. Alternatively, Microwave Imaging via Space-Time (MIST) beamforming technique [11, 12], uses filters that compensate for dispersion and fractional time delays.

Here, in contrast to conventional approaches based on Finite Difference Time Domain (FDTD) methods, the propagation phenomena of UWB signal in human tissue will be investigated analytically. In detail, the body will be modeled as a 3-layer eccentric cylinder of infinite length, and Maxwell's equations will be solved. In addition, the UWB microwave imaging method introduced in [14] will be employed using the analytical results. As stated earlier, the method is based on the Huygens Principle; using HP to forward propagate the waves removes the need to solve inverse problems, which in turn, removes the need for matrix generation/inversion. Furthermore, UWB allows the utilization of all the information in the frequency domain by combining the information from the individual frequencies, resulting in the construction of a consistent image. It follows that the methodology can identify the presence and location of significant scatterers inside a multilayered volume without having apriori knowledge on the dielectric properties of the target object.

Previously, the authors have performed successful simulation and

measurement tests to validate the HP on canonical objects with single and multiple eccentric inclusions [14–16]. In this paper, stratified cylinders involving at least 3 different layers are used as models in both simulations and measurements. Potential applications of this method includes breast cancer detection, internal organ imaging, and whole body imaging. The paper is organized as follows. In section II Maxwell's equations are solved for a 3-layer stratified eccentric cylinder model. In Section III the HP based procedure is reviewed, and the procedure is verified through realistic simulations in Section IV. Validation of the method through measurements on a multi-layered cylinder is given in Section IV, and finally Section V concludes the paper.

## 2. 3-LAYER STRATIFIED ECCENTRIC CYLINDER

Here, we consider a 3-layer stratified cylinder in free space, illuminated by a plane wave having a frequency $f$. The three cylinders are indicated as cylinder '0', cylinder '1' and cylinder '2', and have radiuses $a_0$, $a_1$ and $a_2$ respectively (see fig. 1).

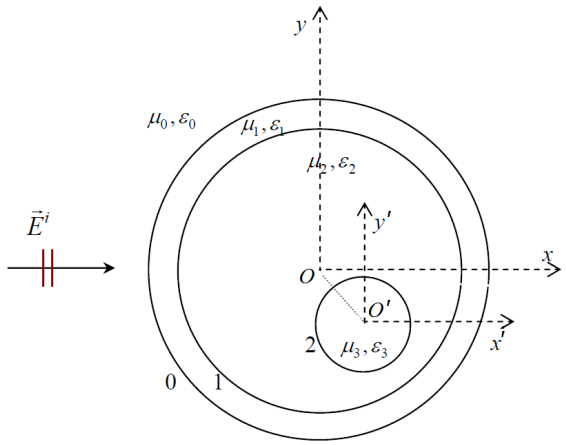


**Figure 1.** 3-layer stratified eccentric cylinder in free space.

Cylinder '0' is characterized by $\varepsilon_1$,$\mu_1$, both of which can be complex and can vary with the frequency. Thus we have:

$$k_1 = \omega\sqrt{\varepsilon_1\mu_1}, \qquad \omega = 2\pi f \tag{1a}$$

$$Z_1 = \sqrt{\frac{\mu_1}{\varepsilon_1}} \tag{1b}$$

Cylinder '1' is characterized by $\varepsilon_2$,$\mu_2$, both of which can be complex and can vary with the frequency. It holds:

$$k_2 = \omega\sqrt{\varepsilon_2\mu_2} \tag{2a}$$

$$Z_2 = \sqrt{\frac{\mu_2}{\varepsilon_2}} \tag{2b}$$

Cylinder '2' is characterized by $\varepsilon_3$,$\mu_3$, both of which can be complex and can vary with the frequency. Such that:

$$k_3 = \omega\sqrt{\varepsilon_3\mu_3} \tag{3a}$$

$$Z_3 = \sqrt{\frac{\mu_3}{\varepsilon_3}} \tag{3b}$$

To determine the field in different regions, we start by writing the field expressions for axial components, where $\phi_0$ represents the angle of incidence of the plane wave.

$$E_z^0 = E_0 \sum_{n=-\infty}^{+\infty} (-j)^n [J_n(k_0\rho) + o_{0,n} H_n^{(2)}(k_0\rho)] e^{jn(\phi-\phi_0)}, \qquad \rho > a_0 \tag{4a}$$

$$E_z^1 = E_0 \sum_{n=-\infty}^{+\infty} (-j)^n [i_{1,n} J_n(k_1\rho) + o_{1,n} H_n^{(2)}(k_1\rho)] e^{jn\phi}, \qquad a_1 < \rho < a_0 \tag{4b}$$

$$E_z^2 = E_0 \sum_{n=-\infty}^{+\infty} (-j)^n [i_{2,n} J_n(k_2\rho') + o_{2,n} H_n^{(2)}(k_2\rho')] e^{jn\phi'}, \qquad \rho < a_1 \text{ and } \rho' > a_2 \tag{4c}$$

$$E_z^3 = E_0 \sum_{n=-\infty}^{+\infty} (-j)^n i_{3,n} J_n(k_3\rho') e^{jn\phi'}, \qquad \rho' < a_2 \tag{4d}$$

Equations (4) hold in free-space, inside cylinder '0', inside cylinder '1' and inside cylinder '2', respectively. Similarly we have the following field expressions for azimuthal components:

$$H_{\phi}^{0} = \frac{E_0}{jZ_0} \sum_{n=-\infty}^{+\infty} (-j)^n [J'_n(k_0\rho) + o_{0,n} H'^{(2)}_n(k_0\rho)] e^{jn(\phi-\phi_0)}, \quad \rho > a_0 \tag{5a}$$

$$H_{\phi}^{1} = \frac{E_0}{jZ_1} \sum_{n=-\infty}^{+\infty} (-j)^n [i_{1,n} J'_n(k_1\rho) + o_{1,n} H'^{(2)}_n(k_1\rho)] e^{jn\phi}, \quad a_1 < \rho < a_0 \tag{5b}$$

$$H_{\phi'}^{2} = \frac{E_0}{jZ_2} \sum_{n=-\infty}^{+\infty} (-j)^n [i_{2,n} J'_n(k_2\rho') + o_{2,n} H'^{(2)}_n(k_2\rho')] e^{jn\phi'}, \quad \rho < a_1 \text{ and } \rho' > a_2 \tag{5c}$$

$$H_{\phi'}^{3} = \frac{E_0}{jZ_3} \sum_{n=-\infty}^{+\infty} (-j)^n i_{3,n} J'_n(k_3\rho') e^{jn\phi'}, \quad \rho' < a_2 \tag{5d}$$

By applying the boundary condition at $\rho = a_0$ we have:

$$\begin{aligned} E_z^0(\rho = a_0) = E_z^1(\rho = a_0) \;\Rightarrow \\ [J_n(k_0 a_0) + o_{0,n} H_n^{(2)}(k_0 a_0)] e^{-jn\phi_0} \\ = i_{1,n} J_n(k_1 a_0) + o_{1,n} H_n^{(2)}(k_1 a_0) \end{aligned} \tag{6a}$$

$$\begin{aligned} H_{\phi}^0(\rho = a_0) = H_{\phi}^1(\rho = a_0) \;\Rightarrow \\ [J'_n(k_0 a_0) + o_{0,n} H'^{(2)}_n(k_0 a_0)] e^{-jn\phi_0} \\ = \frac{Z_0}{Z_1} [i_{1,n} J'_n(k_1 a_0) + o_{1,n} H'^{(2)}_n(k_1 a_0)] \end{aligned} \tag{6b}$$

From (6a) and (6b),

$$i_{1,n} = R_n + o_{0,n} S_n \tag{7a}$$

$$o_{1,n} = \overline{R}_n + o_{0,n}\overline{S}_n \tag{7b}$$

where, $R_n$, $S_n$, $\overline{R}_n$ and $\overline{S}_n$ are calculated after solving system of (6a) and (6b).

Next, applying the boundary condition at $\rho' = a_2$ we have:

$$\begin{aligned} &E_z^2(\rho' = a_2) = E_z^3(\rho' = a_2) \;\Rightarrow \\ &i_{2,n}J_n(k_2a_2) + o_{2,n}H_n^{(2)}(k_2a_2) = i_{3,n}J_n(k_3a_2) \end{aligned} \tag{8a}$$

$$\begin{aligned} &H_{\phi'}^2(\rho' = a_2) = H_{\phi'}^3(\rho' = a_2) \;\Rightarrow \\ &i_{2,n}J_n'(k_2a_2) + o_{2,n}H'^{(2)}_n(k_2a_2) = \frac{Z_2}{Z_3}i_{3,n}J_n'(k_3a_2) \end{aligned} \tag{8b}$$

From (8a) and (8b),

$$o_{2,n} = -i_{2,n}Q_n \tag{9}$$

where $Q_n$ can be determined by manipulating (8). To facilitate the imposition of boundary conditions at $\rho = a_1$, $E_z^2$ and $H_{\phi'}^2$ are first expressed in terms of $\rho$ and $\phi$.

$$\begin{aligned} E_z^2 =& E_0\sum_{n=-\infty}^{+\infty}(-j)^n[i_{2,n}\sum_{m=-\infty}^{+\infty}J_{m-n}(k_2d)J_m(k_2\rho)e^{jm\phi}e^{-j(m-n)\overline{\phi}} \\ &+ o_{2,n}\sum_{m=-\infty}^{+\infty}H_m^{(2)}(k_2\rho)J_{m-n}(k_2d)e^{jm\phi}e^{-j(m-n)\overline{\phi}}], \\ &\rho < a_1 \text{ and } \rho' > a_2 \end{aligned} \tag{10a}$$

$$\begin{aligned} H_{\phi'}^2 =& \frac{E_0}{jZ_2}\sum_{n=-\infty}^{+\infty}(-j)^nE_0[i_{2,n}\sum_{m=-\infty}^{+\infty}J_{m-n}(k_2d)J_m'(k_2\rho)e^{jm\phi} \\ &e^{-j(m-n)\overline{\phi}} + o_{2,n}\sum_{m=-\infty}^{+\infty}H'^{(2)}_m(k_2\rho)J_{m-n}(k_2d)e^{jm\phi}e^{-j(m-n)\overline{\phi}}], \\ &\rho < a_1 \text{ and } \rho^{'} > a_2 \end{aligned} \tag{10b}$$

In above, $d$ and $\overline{\phi}$ represent the distance between the axes of cylinders '1' and '2' ($OO'$) and the angle between $OO'$ and the x-axis, respectively.

Moving on to the boundary condition at $\rho = a_1$, we have:

$$E_z^1(\rho = a_1) = E_z^2(\rho = a_1) \quad \Rightarrow$$
$$\sum_{n=-\infty}^{+\infty} (-j)^n [i_{1,n} J_n(k_1 a_1) + o_{1,n} H_n^{(2)}(k_1 a_1)] e^{jn\phi}$$
$$= \sum_{n=-\infty}^{+\infty} (-j)^n [i_{2,n} \sum_{m=-\infty}^{+\infty} J_{m-n}(k_2 d) J_m(k_2 a_1) e^{jm\phi} e^{-j(m-n)\overline{\phi}}$$
$$+ o_{2,n} \sum_{m=-\infty}^{+\infty} H_m^{(2)}(k_2 a_1) J_{m-n}(k_2 d) e^{jm\phi} e^{-j(m-n)\overline{\phi}}] \tag{11a}$$

$$H_\phi^1(\rho = a_1) = H_\phi^2(\rho = a_1) \quad \Rightarrow$$
$$\sum_{n=-\infty}^{+\infty} (-j)^n [i_{1,n} J_n'(k_1 a_1) + o_{1,n} H'^{(2)}_n(k_1 a_1)] e^{jn\phi}$$
$$= \frac{Z_1}{Z_2} \sum_{n=-\infty}^{+\infty} (-j)^n [i_{2,n} \sum_{m=-\infty}^{+\infty} J_{m-n}(k_2 d) J_m'(k_2 a_1) e^{jm\phi}$$
$$e^{-j(m-n)\overline{\phi}} + o_{2,n} \sum_{m=-\infty}^{+\infty} H' m^{(2)}(k_2 a_1) J_{m-n}(k_2 d) e^{jm\phi}$$
$$e^{-j(m-n)\overline{\phi}}] \tag{11b}$$

Employing the orthogonality property of $e^{-jl\phi}$ ($\int_0^{2\pi} e^{-jl\phi} e^{jm\phi} d\phi = 2\pi$ if $l = m$ and $= 0$ if $l \neq m$), and after some Algebraic manipulation the following result is obtained,

$$\sum_{n=-\infty}^{+\infty} i_{2,n} G_{l,n} = V_l \tag{12}$$

where $G_{l,n}$ and $V_l$ can be determined by manipulating (11), after a proper truncation.

Thus, all inward and outward fields, and hence the field everywhere inside the stratified cylinder have been calculated. It should be noted that if the cylinder (fig. 1) is illuminated by an electrical z-directed line source of intensity $I$, then all the expressions in this section which have been derived from the plane wave illumination

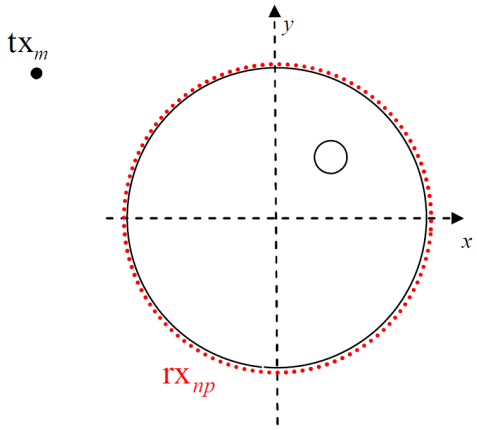


**Figure 2.** Pictorial view of the problem.

can still be used by simply replacing $(-j)^n$ with $H_n^{(2)}(k_0\rho_0)$, where $\rho_0$ represents the distance of the line source from the axis of the cylinder.

## 3. THE HUYGENS PRINCIPLE-BASED PROCEDURE

In this section, we briefly recall the HP based procedure. The reader can refer to [14] for more details. Let us consider a cylinder with a radius $a_0$ in free space. The cylinder is illuminated by a transmitting line source $\text{tx}_m$ and operates at a frequency $f$. At this point, it is assumed that the dielectric properties of the cylinder, i.e. the dielectric constant $\varepsilon_{r1}$ and the conductivity $\sigma_1$ are known. As an inclusion, a smaller cylinder with a higher dielectric constant than $\varepsilon_{r1}$ is placed inside the original cylinder (fig. 2). The problem consists of identifying the presence and location of the inclusion by using only the fields measured outside the cylinder.

Suppose that the field at the surface points $rx_{np} = (a_0, \phi_{np})$ is known, such that:

$$E|_{rx_{np}} = E_{np} \quad \text{with} \quad np = 1, ...N_{PT} \tag{13}$$

where $N_{PT}$ indicates the number of measured points across the outside cylinder. We calculate the field inside the cylinder as the superposition of the fields radiated by the $N_{PT}$ observation points of (13):

$$E_{\text{HP}}^{\text{rcstr}}(\rho, \phi; tx; f) = \Delta_s \sum_{np=1}^{N_{PT}} E_{np} G(k_1 |\overrightarrow{\rho}_{np} - \overrightarrow{\rho}|) \tag{14}$$

where $G(k_1|\overrightarrow{\rho}_{np} - \overrightarrow{\rho}|)$ is the Green's function defined in [14], $(\rho, \phi) \equiv \overrightarrow{\rho}$ is the observation point, $k_1$ represents the wave number for the media constituting the cylinder and $\Delta_s$ is the spatial sampling value. In (14), the string "rcstr" is used to indicate the reconstructed internal field, while the string HP indicates that a HP-based procedure will be employed; additionally, we note that the reconstructed field will depend on the illuminating source and the frequency (since $E_{np}$ depends on these parameters). It has been shown that a mismatch appears in the region of transmission of the two media. Thus, assuming we have $M$ transmitting sources $\text{tx}_m$ with $m = 1, 2...M$, and $N_F$ frequencies $f_i$, the intensity of the resulting image $I$ using the Green's functions can be obtained through:

$$I_{HP}(\rho, \phi) = \frac{1}{B} \sum_{m=1}^{M} \sum_{i=1}^{N_F} \Delta_f |E_{HP}^{rcstr}(\rho, \phi; tx; f_i)|^2 \tag{15}$$

In (15), $\Delta_f$ and $B$ represent the frequency and the bandwidth, respectively. The resolution is expected to achieve the optical resolution limit of $\lambda_{f_{\max}}/4$, where $\lambda_{f_{\max}}$ represents the wavelength in the cylinder calculated at the highest employed frequency. During the initial simulations, it was observed that an image of the transmitter appeared in the result, which sometimes masked the area of interest. However, this transmitter image can be successfully removed by modifying (14) such that:

$$E_{HP}^{\text{rcstr}}(\rho, \phi; tx; f) = \Delta_s \sum_{np=1}^{N_{PT}} (E_{np} - \text{avg}_M\{E_{np}\}) G(k_1|\overrightarrow{\rho}_{np} - \overrightarrow{\rho}|) \tag{16}$$

where $\text{avg}_M\{E_{np}\}$ represents the average of signals obtained illuminating the object using $M$ different transmitter positions. This in effect "smears" out the transmitter image.

## 4. VALIDATION THROUGH SIMULATION: MULTILAYERED OBJECT WITH AN ECCENTRIC INCLUSION

Before proceeding to perform an experiment, the applicability of the analytical formulation was tested by simulating a 3-layer cylindrical object with an eccentric inclusion. To verify this using the HP procedure, an external Agar cylinder in free space having a radius of 4.25 cm, with electrical properties (frequency independent for the

moment) of $\varepsilon_{r1} = 70$ and $\sigma_1 = 0.5$ S/m, with inclusions is considered. A smaller cylinder of radius 3 cm, with the same dielectric constant value but a higher conductivity value $\sigma_1 = 2$ S/m is placed inside the outer cylinder to represent the second medium. Finally, an eccentric inclusion made of a Perfectly Electrically Conducting (PEC) cylinder of radius 3 mm, is placed 1.75 cm away from the axis of the cylinder, 90° degrees relative to the x-axis.

The external cylinder is illuminated using 4 transmitter sources situated 8 cm from the axis of the cylinder, while a frequency band of 1-3 GHz with frequency spacing of 10 MHz is used. For each illuminating source and for each frequency, the field ($E_{np}$) at $N_{PT} = 120$ points lying on the external surface is calculated. It should be noted that in this example, $E_{np}$ has been determined using the analysis presented in Section II. Finally, the average of the 4 data sets ($\text{avg}_M\{E_{np}\}$) is calculated and the Huygens principle is applied to the difference between the measured field and the average field as stated in (16). Fig 3 shows the normalized intensity obtained through (15) and using an appropriate image adjusting. The image is adjusted by enforcing to zero the intensity values below 0.5 and expanding from 0 to 1 of the values above 0.5. A peak can be clearly detected in the regions of the inclusions: thus, both detection and localization are achieved for this multi-layered problem.

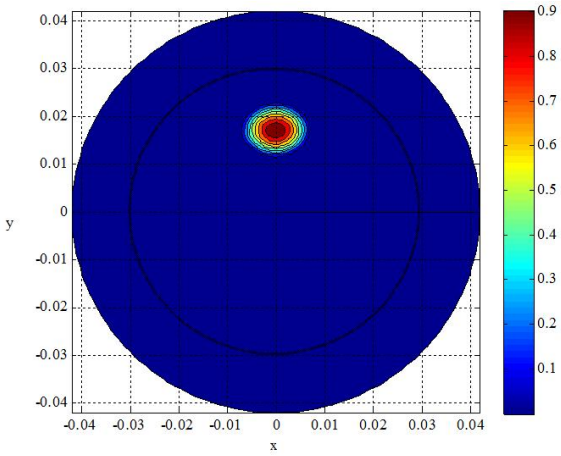


**Figure 3.** Cylinder with an inclusion: normalized intensity obtained through (15). All scales are in meters.

Next, a similar geometrical model, this time with realistic human body tissue properties assigned to its three layers is further simulated.

The external cylinder is assumed to be a thin human skin with radius 4.25 cm, $\varepsilon_{r1} = 41$ and $\sigma_1 = 0.8$ S/m [17]. The internal concentric cylinder and the eccentric inclusion are then assigned the electrical properties of a normal ($\varepsilon_{r1} = 10$ and $\sigma_1 = 0.8$ S/m) and malignant ($\varepsilon_{r1} = 50$ and $\sigma_1 = 1$ S/m) tissue respectively. In the simulation, the radius of the middle cylinder is increased to 4.05 cm in order to have a thin skin layer of only 2mm, while the sizes of other layers remain unchanged. The same frequency range, sampling and transmitting sources and other conditions as the previous simulation are implemented here. Figure 4(b) shows the normalized intensity obtained through (15) and using an appropriate image adjusting and averaging. It is important to point out that in this simulation, the quantity $k_2$ is used instead of $k_1$ in the Green's function for the reconstruction process. This is due to the fact that as a thin skin layer is used to represent the outer layer, the target is now contained in the second layer, which represents a normal breast tissue.

A peak can be clearly detected in the region of the inclusion. It an be seen that the method successfully detects and locates the breast tumor in this multilayered simulation, and knowing that malignant breast tissue has a conductivity value higher than most human tissues [18], its detection will be achieved in nearly all cases.

Next, an analysis of the signal to clutter ratio and resolution with respect to the band is performed. Specifically, We define the signal to clutter ratio (S/C) as the ratio between the maximum inclusion response and the maximum clutter response in the same image [10]. To evaluate the S/C with respect to the band, we apply (15) for different bandwidths; more in detail, we perform image reconstruction assuming a bandwidth of 1, 2, and 4 GHz (the lower frequency is fixed at 1 GHz). Next, for each image the S/C is calculated and reported in table I. Note that in HP procedure the within-breast S/C approaches 4 dB for a bandwidth of 4 GHz. This value has been obtained with $M$=4 transmitter positions, $N_{PT}$=120, and a frequency sampling of 20 MHz. The reader is invited to refer to [14] for further detail concerning variation of S/C with respect to $M$, $N_{PT}$ and frequency sampling. In the same paper, it has been shown that an increase of approximately 4 dB occurs if using $M$=12. Note that in [10], for a similar problem of 4 GHz bandwidth, a within-breast S/C of 4.1 dB has been obtained by employing the delay-and-sum beamforming algorithm and using $M$ =45, while in [19] a within-breast S/C of 4 dB has been obtained by employing time reversal approach and using $M$=7. Note that in both [10] and [19], the skin has also been considered.

Resolution, i.e. the dimension of the region whose normalized intensity is above 0.5, has been addressed with respect to the band.

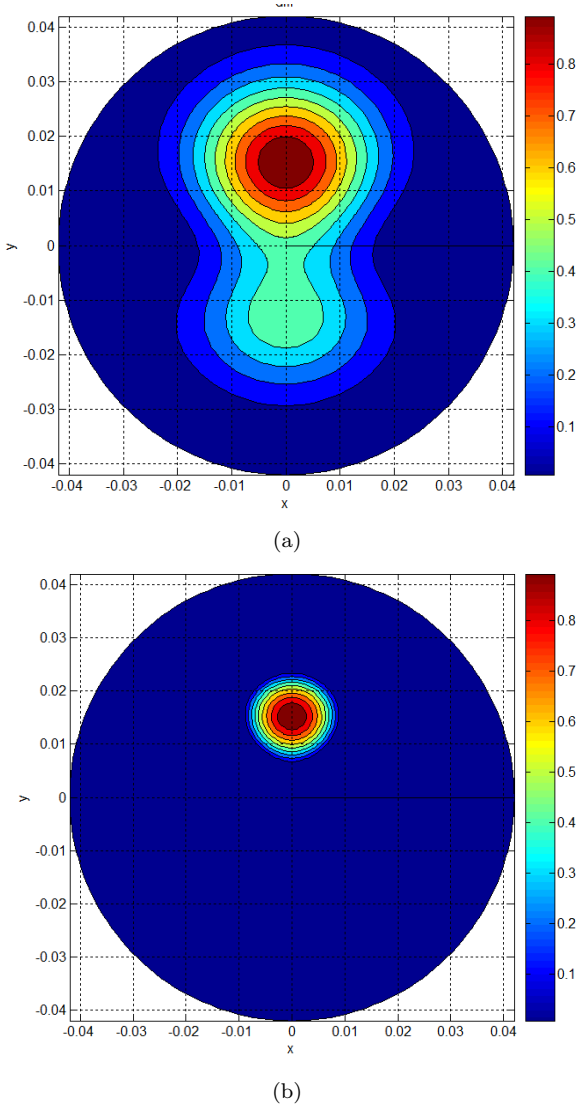


(a)

(b)

**Figure 4.** Normalized intensity obtained through (15), (a) before image adjusting, (b) after image adjusting. All scales are in meters.

Specifically, in the same Table I the resolution is given assuming a bandwidth of 1, 2 and 4, respectively. It can be shown (see Table I) that the resolution achieves the optical resolution limit of $\lambda_{f_{\max}}/4$; this value is better than that achieved by time reversal approach [19]

and comparable to that achieved by the delay-and-sum beamforming algorithm [10]. A detailed analysis on computational time can be found in [14].

**Table 1.** Within-breast S/C and Resolution for bandwidth of 1,2,4 GHz.

| Band (GHz) | Within-breast S/C (dB) | Resolution (mm) |
|---|---|---|
| 1 | 3 | 7.5 |
| 2 | 3.5 | 6 |
| 4 | 3.9 | 5 |

## 5. VALIDATION THROUGH MEASUREMENTS: MULTILAYERED OBJECT WITH AN ECCENTRIC INCLUSION

To access the practical ability of the HP method in locating an eccentric inclusion in a multi-layered medium, a human tissue like model was constructed. To achieve this purpose, a 2 mm thick PVC cylindrical pipe with radius of 5 cm was concentrically placed inside a larger plastic pipe, also 2 mm thick but with a larger radius of 6.25 cm. Both pipes were filled with agar-agar gel approximating a high water-content human tissue; a 3mm thick PEC rod representing a tumor was positioned eccentrically inside the gel [fig. 5(a)], at a distance of 3.25 cm from the axis of the cylinders [fig. 5(b)]. Although the thickness of the pipes was chosen to be as narrow as possible (2 mm), their minimal effect on the imaging procedure could not be ignored, making this model effectively a 5-layered problem.

The agar-agar was dissolved in hot water at approximately 95°C and then cooled to room temperature to form a semi-transparent jell. The dielectric constant and the conductivity are functions of the concentration of the agar-agar [20]; for this experiment two distinct concentrations of Agar were used. The external plastic pipe was filled with a lower conductive Agar ($\sigma_1 = 0.5$), while the smaller plastic pipe was filled with a higher conductive Agar ($\sigma_1 = 2$). This increase in conductivity value was gained by adding the necessary amount of salt to the original Agar mixture, whilst the change in the dielectric constant value was not notable and was considered to be equal to 70 for both agar solutions. By comparing these values with those given in [18], it can be noted that the dielectric constant and the conductivity of agar-agar are similar to the actual dielectric properties of human tissues. It is worthwhile to point out that the loss-tangent of the agar-agar is even greater than that encountered in some human tissue

(a)

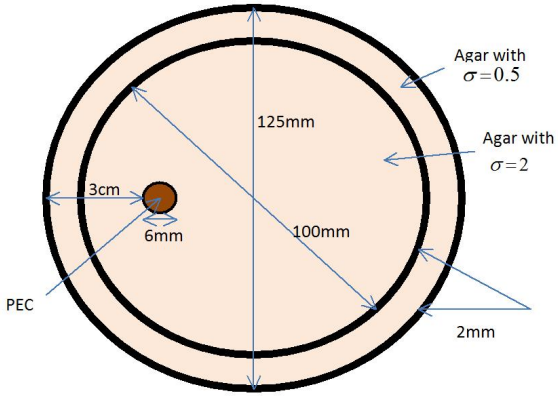


(b)

**Figure 5.** (a) Multilayered medium with an inclusion, (b) Pictorial view of the problem

imaging problems; thus, it follows that the example here presented can be considered representative of lossy media imaging problems.

Frequency-domain UWB measurements were performed in free-space, using a Vector Network Analyzer (VNA) arrangement to obtain the transfer function. Discone antennas, vertically polarized and omni-directional in the azimuth plane were used, after calibration. In order to observe the variation of signal in different frequencies, the

measurements were recorded using a large frequency range of 1-10 GHz, using a frequency step of 5.6 MHz. For each set of measurements, the location of the transmitting antenna was fixed at approximately 15 cm away from the axis of the cylinder, while the receiver antenna was positioned roughly 1 cm away from the external surface of the agar-agar cylinder and mounted on a computer-controlled rotating stage with 3 degrees of angular resolution. In addition, a 30 dB amplifier was used to increase the received signal.

Next, the field $E_{np}$ at $N_{PT} = 120$ equally *phi*-spaced points lying on the external surface was measured; it should be noted that the employed number of points leads to a spatial sampling of approximately $0.1\lambda_{1,f_{\max}}$, where $\lambda_{1,f_{\max}}$ represents the wavelength in the P.M.M.A cylinder calculated at the highest frequency (10 GHz). It has been shown that the number of measured points and the frequency samples can be reduced without decreasing the detection capability [15]. Four sets of data were recorded, changing the position of the transmitting antenna along *phi* with a step of 90 degrees. Next, the average of the 4 data sets ($\text{avg}_M\{E_{np}\}$) is calculated and the Huygens principle is applied to the difference between the measured field and the average field as stated in (16). However, when applying the Green's function in the reconstruction process, $k_0$ is now used. This is done due to the fact that the cylinder containing the target was placed in free-space and the receiving antenna was not completing touching the measurement grid, and hence the initial use of $k_1$ resulted in some distortion. It was then observed that the use of $k_0$ not only resulted in detection of the target, but also excellent positioning. Furthermore, the use of $k_0$ removes the need of having any knowledge about the dielectric properties of the target volume. Figure 6(b) shows the normalized intensity obtained through (15) and using an appropriate image adjusting. The image is adjusted by enforcing to zero the intensity values below 0.5 and expanding from 0 to 1 of the values above 0.5. A peak can be clearly detected in the region of the inclusion: thus, both detection and localization are achieved for this multi-layered problem.

## 6. CONCLUSIONS

In this paper, the analysis of a novel microwave imaging procedure based on Huygens principle has been extended to multilayered mediums. Specifically, a complete analytical process based on the exact Maxwell solution for a multi-layered eccentric cylinder has been formulated. The model assumes that the body can be approximated as a stratified multi-layered cylinder with an eccentric inclusion representing a tumor. The analytical model has been used for

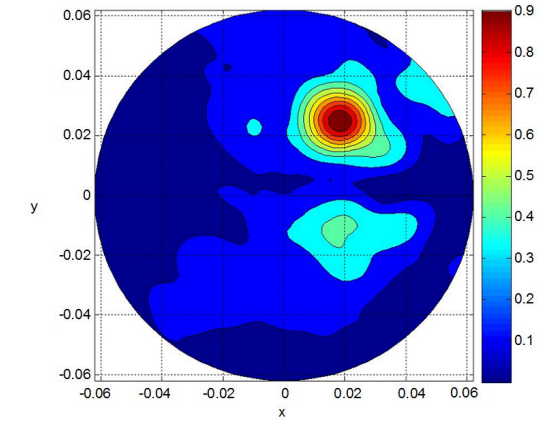


(a)

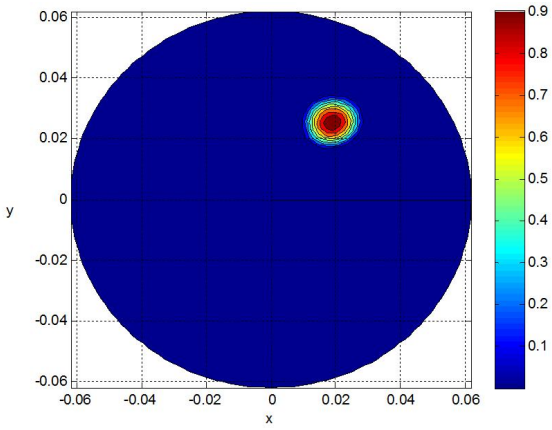


(b)

**Figure 6.** Normalized intensity obtained through (15), (a) before image adjusting, (b) after image adjusting. All scales are in meters.

verifying HP procedure through simulations. Analyzing the S/C and the resolution of the simulated model shows that HP method provides better performance when compared to conventional time-domain approaches. Additionally, the HP has been tested through measurements using a multilayered phantom constituting of human-like tissues containing an inclusion. It has been shown that the HP can detect and locate an inclusion in multilayered cylindrical mediums. Measurements are currently being carried out on a commercial 3D

inhomogeneous breast phantom with many inclusions, to further move towards solving more realistic medical imaging problems.

## ACKNOWLEDGMENT

This research was partially supported by UK Engineering and Physical Sciences Research Council and partially supported by a Marie Curie Intra European Fellowship within the 7th European Community Framework Program.

## REFERENCES

1. P. M. Meaney and K. D. Paulsen, "Nonactive antenna compensation for fixed-array microwave imaging: Part IIImaging results," *IEEE Trans. Med. Imag.*, vol. 18, no. 6, pp. 508518, Jun. 1999.
2. D. W. Winters, B. D. Van Veen and S. C. Hagness, "A Sparsity Regularization Approach to the Electromagnetic Inverse Scattering Problem", *IEEE Transactions on Antennas and Propagation*, Vol. 58, No. 1, Jan 2010, pp. 145-154.
3. M. Donelli, I. Craddock, D. Gibbins, and M. Sarafianou, "A Three-Dimensional Time Domain Microwave Imaging Method for Breast Cancer Detection Based on an Evolutionary Algorithm", *Progress In Electromagnetics Research M*, Vol. 18, pp. 179-195, 2011.
4. S. Kusiak and J. Sylvester, "The scattering support," Comm. Pure Appl. Math., vol. 56, no. 11, pp. 1525 1548, 2003.
5. S. Kusiak and J. Sylvester, "The convex scattering support in a background medium," *SIAM J. Math. Anal.*, vol. 36, no. 4, pp. 1142-1148, 2005.
6. M. Chiappe and G. L. Gragnani, "An analytical approach to the reconstruction of the radiating currents in inverse electromagnetic scattering", *Microwave and Optical Technology Letters*, vol. 49, n. 2, pp. 354-360, February 2007.
7. G. L. Gragnani, "Two-dimensional non-radiating currents for imaging systems: theoretical development and preliminary assessment", *IET Microwaves, Antennas and Propagation*, vol. 3, n. 8, pp. 1164-1171, December 2009.
8. X. Li and S. C. Hagness, "A confocal microwave imaging algorithm for breast cancer detection," *IEEE Microw. Wireless Compon. Lett.*, vol. 11, no. 3, pp. 130132, Mar. 2001.

9. A. Lazaro, D. Girbau and R. Villarino, " Simulated and Experimental Investigation of Microwave Imaging Using UWB", *Progress In Electromagnetics Research*, PIER 94, 263-280, 2009.
10. E. C. Fear, X. Li, S. C. Hagness, and M. A. Stuchly, "Confocal microwave imaging for breast cancer detection: Localization of tumors in three dimensions," *IEEE Trans. Biomed. Eng.*, vol. 4, no. 8, pp. 812822, Aug. 2002.
11. E. J. Bond, X. Li, S. C. Hagness, and B. D. Van Veen, "Microwave imaging via space-time beamforming for early detection of breast cancer," *IEEE Transactions on Antennas and Propagation*, vol. 51, no. 8, pp. 16901705, Aug. 2003.
12. X. Li, S. K. Davis, S. C. Hagness, D. W. van der Weide, and B. D. Van Veen, "Microwave imaging via space-time beamforming: Experimental investigation of tumor detection inmultilayer breast phantoms," *IEEE Transactions on Microwave Theory and Techniques*, vol. 52, no. 8, pp. 18561865, Aug. 2004.
13. M. Klemm, I. J. Craddock, J.A. Leendertz,A. Preece, and R. Benjamin, "Radar-based breast cancer detection using a hemispherical antenna arrayExperimental results," *IEEE Transactions on Antennas and Propagation*, vol. 57, no. 6, pp. 16921704, Jun. 2009.
14. N. Ghavami, G. Tiberi, D. J. Edwards, and A. Monorchio, "UWB Microwave Imaging of Objects With Canonical Shape," *IEEE Transactions on Antennas and Propagation*, vol.60, no.1, pp.231-239, Jan. 2012.
15. G. Tiberi, N. Ghavami, D. J. Edwards, and A. Monorchio, "Ultrawideband microwave imaging of cylindrical objects with inclusions," *Microwaves, Antennas & Propagation, IET* , vol.5, no.12, pp.1440-1446, September 16 2011.
16. G. Tiberi, N. Ghavami, D. J. Edwards, and A. Monorchio, "Novel Techniques for UWB Microwave Imaging of Objects with Canonical Shape", *PIERS Proceedings*, Marrakesh, Morocco, 2011.
17. X. Li, S. K. Davis, S. C. Hagness, D. W. van der Weide, and B. D. Van Veen, "Microwave imaging via space-time beamforming: Experimental investigation of tumor detection in multilayer breast phantoms," *IEEE Trans. Microwave Theory Tech.*, vol. 52, no. 8, pp. 1856-1865, Aug. 2004.
18. C. Gabriel, S. Gabriely and E. Corthout, "The Dielectric Properties of Various Tissues" *Phys. Med. Biol.*, Vol. 41, p.p. 2231-2249, Year: 1996.
19. Y. Chen, E. Gunawan, K. S. Low, S. Wang, Y. Kim, C. B.

Soh, "Pulse Design for Time Reversal Method as Applied to Ultrawideband Microwave Breast Cancer Detection: A Two-Dimensional Analysis", *IEEE Transactions on Antennas and Propagation*, Vol. 55, Issue: 1, Publication Year: 2007, Page(s): 194 - 204

20. K. Iizuka, "An agar-agar chamber for study of electromagnetic waves in an inhomogeneous medium", *IEEE Transactions on Antennas and Propagation*,Vol. 19 , Issue: 3, Year: 1971 , Page(s): 365 - 377